applied sciences

MDPI

Article

Image Human Thorax Using Ultrasound Traveltime Tomography with Supervised Descent Method

Tong Zhang, Rui Guo, Haolin Zhang, Hongyu Zhou, Yeyu Cao, Maokun Li *, Fan Yang and Shenheng Xu

Beijing National Research Center for Information Science and Technology (BNRist), Institute for Precision Medicine, Department of Electronic Engineering, Tsinghua University, Beijing 100084, China; t-zhang20@mails.tsinghua.edu.cn (T.Z.); guor93@tsinghua.edu.cn (R.G.); zhanghl13@tsinghua.org.cn (H.Z.); zhouhy21@mails.tsinghua.edu.cn (H.Z.); yy-cao19@mails.tsinghua.edu.cn (Y.C.); fan_yang@tsinghua.edu.cn (F.Y.); shxu@tsinghua.edu.cn (S.X.)

* Correspondence: maokunli@tsinghua.edu.cn

Abstract: The change of acoustic velocity in the human thorax reflects the functional status of the respiratory system. Imaging the thorax's acoustic velocity distribution can be used to monitor the respiratory system. In this paper, the feasibility of imaging the human thorax using ultrasound traveltime tomography with a supervised descent method (SDM) is studied. The forward modeling is computed using the shortest path ray tracing (SPR) method. The training model is composed of homogeneous acoustic velocity background and a high-velocity rectangular block moving in the domain of interest (DoI). The average descent direction is learned from the training set. Numerical experiments are conducted to verify the method's feasibility. Normal thorax model experiment proves that SDM traveltime tomography can efficiently reconstruct thorax acoustic velocity distribution. Numerical experiments based on synthetic thorax model of pleural effusion and pneumothorax show that SDM traveltime tomography has good generalization ability and can detect the change of acoustic velocity in human thorax. This method might be helpful for the diagnosis and evaluation of respiratory diseases.

Keywords: thorax imaging; ultrasound traveltime tomography; supervised descent method

check for updates

Citation: Zhang, T.; Guo, R.; Zhang, H.; Zhou, H.; Cao, Y.; Li, M.; Yang, F.; Xu, S. Imaging Human Thorax Using Ultrasound Traveltime Tomography with Supervised Descent Method. *Appl. Sci.* **2022**, *12*, 6763. https://doi.org/10.3390/app12136763

Academic Editor: Nikolaos Dikaios

Received: 30 April 2022
Accepted: 29 June 2022
Published: 4 July 2022

Publisher's Note: MDPI stays neutral with regard to jurisdictional claims in published maps and institutional affiliations.

Copyright: © 2022 by the authors. Licensee MDPI, Basel, Switzerland. This article is an open access article distributed under the terms and conditions of the Creative Commons Attribution (CC BY) license (https://creativecommons.org/licenses/by/4.0/).

1. Introduction

Ultrasound imaging is widely used in industrial and biomedical imaging. Industrial imaging is important in nondestructive evaluation (NDE) [1]. It can be used to evaluate the health of material [2–5]. The information of liquid flow can also be obtained by ultrasound imaging [6–8]. In the medical field, ultrasound imaging is widely used for its low-cost, portability, radiationless, and real-time compared with other imaging methods, such as computed tomography (CT) and magnetic resonance imaging (MRI). Ultrasound is applied to imaging heart [9–11], liver [12,13], brain [14–16] and many other human parts [17]. In most cases, ultrasound imaging is realized by transmitting ultrasound at megahertz into the human body and analyzing the reflected signal. However, this workflow is hard to implement in thorax imaging, because complex reflection and refraction occur at the lung-pleura interface and among the millions of alveoli inside the lungs, resulting in both chaotic and low-energy reflected signal [18]. In addition, the high frequency will cause severe attenuation, resulting in the reflected signal's low signal-to-noise ratio (SNR). Current thorax imaging methods include X-ray [19], CT [20], MRI [21], and electrical impedance tomography (EIT) [22]. Microwave thorax imaging is still in the research stage [23]. These methods all have limitations. The radiation from CT and X-rays is harmful to human health. The equipment of MRI is not portable and its imaging quality is not that good because of the air in the lung. The resolution of EIT and microwave imaging is relatively low.

Though the reflected signal can hardly be used for thorax imaging, it contains information about the thorax state. B-lines are suggested to originate as ring-down artifacts from

irregularities at the lung–pleura interface, which contains information inside the thorax and correlates with a variety of respiratory diseases [24]. However, the results obtained from B-lines remain qualitative, subjective, and suboptimal [25]. In addition, information in the frequency domain can be used to diagnose pulmonary fibrosis quantitatively [25]. Ultrasound can also be used to monitor the states of the respiratory system, see [26–28]. In addition to reflected signal, transmission signal can be applied to thorax examination. Transmission signal is the signal that propagates through the human thorax. Acoustic wave can permeate human thorax as long as the frequency is low enough. According to Rueter et al. [29], the propagation of acoustic wave in human thorax shows three distinct bands according to frequency. Sound of frequency around 1 kHz can propagate in human thorax at velocity of 30–50 m/s. At this band, the thorax model is established and verified by simulations and experiments, see [30,31]. The feasibility of diagnosing pulmonary diseases using sound at this band is also researched, see [32,33]. Sound of frequency between 1 and 10 kHz is hard to permeate thorax. Ultrasound with frequency between 10 kHz and 750 kHz can permeate human thorax at velocity of about 1500 m/s. An ultrasound at this band permits monitoring of the human respiratory system. The transmission ultrasound signal can be analyzed directly for diagnosing lung diseases, see [34,35]. In addition, the transmission ultrasound signal can be used to conduct traveltime tomography. This method is successfully implemented on breast imaging, see [36,37]. So far, to the best knowledge of the authors, traveltime tomography for thorax has not been well studied.

Ultrasound traveltime tomography reconstructs the acoustic velocity distribution from the measured time of the signal traveling from transmitter to receiver. This method is widely used in geophysics. It is robust at low SNR situations [38,39] and can mitigate the challenge aroused by the complexity of ultrasound propagation in complicated media [40,41]. The acoustic velocity is sensitive to the contents of gas, liquid, and their distribution, because their acoustic velocity differs a lot. Thus, it is possible to measure the amount of gas and fluid in the thorax by reconstructing the acoustic velocity distribution, which is crucial in the diagnosis of many diseases [42,43].

Machine learning techniques develop quickly in recent years and it has been widely used in inverse problems. One of the reasons for its popularity is that, through the training process, lots of work can be completed offline, which makes the online predicting process simple and efficient. Supervised descent method is one of these techniques, which is firstly used in face alignment [44]. The average descent direction of the cost function is learned from the training process and used to update the model in the online predicting process. The time-consuming matrix inversion in traditional gradient-based method is no longer needed. Previous studies show that SDM performs well in imaging, such as 2D magnetotelluric imaging [45], microwave thorax imaging [46], EIT thorax imaging [47], and corrosion imaging [48].

In this paper, we study the feasibility of imaging human thorax using ultrasound traveltime tomography with SDM. Numerical experiments based on normal thorax model and synthetic patient thorax model are conducted. The remaining of the paper is organized as follows. In Section 2, the overview of the forward modeling is described. In Section 3, details of traveltime tomography with SDM are discussed. In Section 4, our method is compared with the traditional gradient-based inversion method and its ability to detect the change of acoustic velocity distribution is tested.

2. Forward Modeling for Computing Traveltime

Forward modeling computes traveltime between the transducer T and the receiver R with the given acoustic velocity distribution. The traveltime can be computed as

$$t = \int_T^R \frac{1}{v(\boldsymbol{x})} dl \tag{1}$$

where v is the velocity, $\boldsymbol{x}$ is the position, and dl is the differential length [49]. This non-linear function can be solved by the shortest path ray tracing (SPR) method based on Fermat's

principle. Fermat's principle says that the ultrasonic wave travels along the path that takes the shortest time. SPR converts computing traveltime into finding single-source shortest path in a graph, which can be solved by the Dijkstra algorithm. According to [50], SPR divides the DoI into rectangular elements. Acoustic velocity is defined on the element, which means the velocity in an element is a constant. Nodes are defined on the boundary of elements. Two nodes are connected only when they belong to the same element and are not located on the same element boundary. Figure 1 is an example. The area is divided into $2 \times 2 = 4$ elements, see the dashed squares. Three nodes lie on one edge of the elements. The solid lines are the connections between nodes.

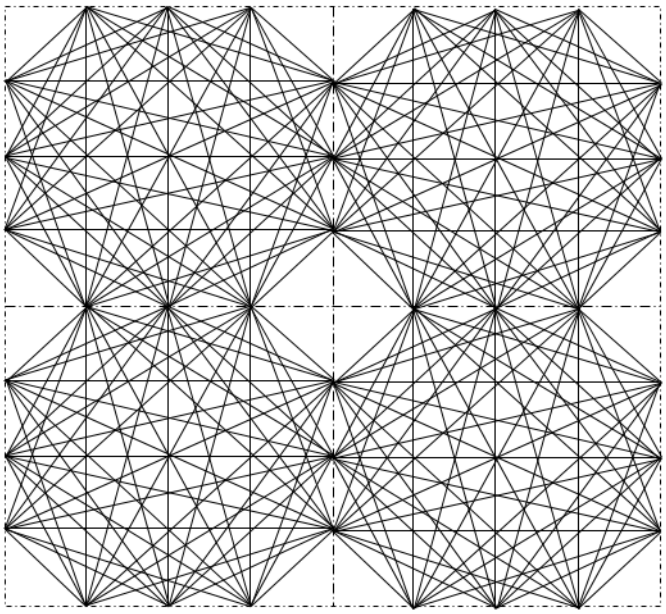

Figure 1. Example of element and possible ray path. Dashed lines: element boundaries. Solid lines: node connections.

The weight of the connection between two nodes is defined as the quotient of their distance and the velocity of the element they belong to. With nodes, connections and weight of connections, an undirected graph is established. Assume t and r is the closest nodes to T and R. Naturally, the shortest path between T and R is the path with the lowest weight between t and r, and the traveltime is the path's weight. The forward modeling can be formulated as:

$$\boldsymbol{d} = F(\boldsymbol{m}) \tag{2}$$

where $\boldsymbol{d}$ is the traveltime data, $\boldsymbol{m}$ is the model including distributions of acoustic velocity and positions of the transducers. With the acoustic velocity distribution, the graph can be constructed. Then, the transducers are assigned to the nodes that are closest to them and the traveltime between them can be calculated by $F(\cdot)$, which is the operator of forward modeling. $F(\cdot)$ calculates traveltime for each transmitter–receiver pair using Dijkstra algorithm.

3. Traveltime Tomography with SDM

3.1. Formulations of Inverse Problem with SDM

Solving the inverse problem is an optimization process to find the best $\boldsymbol{m}$ that minimizes the loss function. The loss function of this problem is defined as

$$L(\boldsymbol{m}) = \|\boldsymbol{d}_{\boldsymbol{obs}} - F(\boldsymbol{m})\|^2 \tag{3}$$

where $\boldsymbol{d_{obs}}$ is the real traveltime data. The Gauss–Newton method can be used to solve this optimization problem [51]. The update of the model can be calculated as

$$\Delta \boldsymbol{m} = \left(\boldsymbol{J}^T \boldsymbol{J}\right)^{-1} \boldsymbol{J}^T (\boldsymbol{d_{obs}} - F(\boldsymbol{m})) = \boldsymbol{K}(\boldsymbol{d_{obs}} - F(\boldsymbol{m})) = \boldsymbol{K}\Delta \boldsymbol{d} \tag{4}$$

where $\boldsymbol{J}$ is the Jacobian matrix of $F(\boldsymbol{m})$ and $\boldsymbol{K} = \left(\boldsymbol{J}^T \boldsymbol{J}\right)^{-1} \boldsymbol{J}^T$ is a mapping from $\Delta \boldsymbol{d}$ to $\Delta \boldsymbol{m}$. The element of Jacobian matrix J_{ik} tells us the change in the ith data point (traveltime) due to a unit change in the kth model parameter (acoustic velocity). In this problem, J_{ik} is non-zero only when the ith path goes through the kth element, and it has an analytical form as

$$J_{ik} = -\frac{s_{ik}}{v_k^2} \tag{5}$$

where s_{ik} is the length of the ith path within the kth element. v_k^2 is the acoustic velocity of the kth element. The update direction $\boldsymbol{K}$ contains the local information of $\boldsymbol{F}$ near $\boldsymbol{m}$. The calculation of K is the key step in Gauss–Newton method, which is also the most time-consuming step, because the calculation of $\boldsymbol{J}$ and matrix inversion take a lot of time. SDM introduces an alternative approach to compute $\boldsymbol{K}$ in a shorter time.

In SDM, $\boldsymbol{K}$ is calculated offline in advance. From Equation (4), the optimization of Equation (3) can be converted to minimize the following function:

$$S = \|\Delta \boldsymbol{m} - \boldsymbol{K}\Delta \boldsymbol{d_{obs}}\|^2 \tag{6}$$

The size of $\Delta \boldsymbol{m}$ and $\boldsymbol{m}$ is $n_{ele} \times 1$, where n_{ele} is the number of elements in the grid, which is also the number of unknowns to be solved. The size of $\boldsymbol{d_{obs}}$ is $n_d \times 1$, where n_d is the number of traveltime data we use. The size of $\boldsymbol{K}$ is $n_{ele} \times n_d$.

We assume that the real model $\boldsymbol{m}$ is in the space expanded by N reference models $\boldsymbol{m^i_{prior}}(i = 1, 2, \cdots, N)$. The corresponding traveltime is $\boldsymbol{d^i_{prior}}$. Then, an average update direction $\tilde{\boldsymbol{K}}$ is calculated by minimizing

$$S^{Tr}(\tilde{\boldsymbol{K}}) = \sum_{i=1}^{N} \left\| \Delta \boldsymbol{m^i_{prior}} - \tilde{\boldsymbol{K}} \Delta \boldsymbol{d^i_{prior}} \right\|^2 \tag{7}$$

where

$$\Delta \boldsymbol{m^i_{prior}} = \boldsymbol{m^i_{prior}} - \boldsymbol{m_0} \tag{8}$$

$$\Delta \boldsymbol{d^i_{prior}} = \boldsymbol{d^i_{prior}} - \boldsymbol{d_0} \tag{9}$$

and $\boldsymbol{m_0}$ is an initial guess of the real model $\boldsymbol{m}$ and $\boldsymbol{d_0} = F(\boldsymbol{m_0})$. The process of computing $\tilde{\boldsymbol{K}}$ offline is called training.

3.2. Offline Training Process

In the training process, the initial model $\boldsymbol{m_0}$ is chosen as homogeneous background. The training set $\boldsymbol{M_{prior}}$ contains N training models. Equation (7) can be written in matrix form as

$$S^{Tr}(\tilde{\boldsymbol{K}}) = \left\| \Delta \boldsymbol{M} - \Delta \boldsymbol{D} \tilde{\boldsymbol{K}}^T \right\|^2 \tag{10}$$

where

$$\boldsymbol{M_{prior}} = \begin{bmatrix} \boldsymbol{m^1_{prior}}^T \\ \boldsymbol{m^2_{prior}}^T \\ \vdots \\ \boldsymbol{m^N_{prior}}^T \end{bmatrix}, \boldsymbol{M_0} = \begin{bmatrix} \boldsymbol{m_0}^T \\ \boldsymbol{m_0}^T \\ \vdots \\ \boldsymbol{m_0}^T \end{bmatrix}, \Delta \boldsymbol{M} = \boldsymbol{M_{prior}} - \boldsymbol{M_0} \tag{11}$$

and

$$\boldsymbol{D_{prior}} = \begin{bmatrix} \boldsymbol{d^1_{prior}}^T \\ \boldsymbol{d^2_{prior}}^T \\ \vdots \\ \boldsymbol{d^N_{prior}}^T \end{bmatrix}, \boldsymbol{D_0} = \begin{bmatrix} \boldsymbol{d_0}^T \\ \boldsymbol{d_0}^T \\ \vdots \\ \boldsymbol{d_0}^T \end{bmatrix}, \Delta \boldsymbol{D} = \boldsymbol{D_{prior}} - \boldsymbol{D_0} \tag{12}$$

Here, the size of $\Delta \boldsymbol{M}$ is $N \times n_{ele}$ and the size of $\Delta \boldsymbol{D}$ is $N \times n_d$. $\tilde{\boldsymbol{K}}$ is a $n_{ele} \times n_d$ matrix.

Because forward modeling of traveltime tomography is non-linear, it takes several iterations to minimize S^{Tr} and learn $\tilde{\boldsymbol{K}}$. The prediction also computes in a iterative way [52]. Thus, in the kth training iteration we have

$$S^{Tr}_k(\tilde{\boldsymbol{K}}) = \left\| \Delta \boldsymbol{M}_k - \Delta \boldsymbol{D}_k \tilde{\boldsymbol{K}}^T_k \right\|^2 \tag{13}$$

where

$$\Delta \boldsymbol{M}_k = \boldsymbol{M_{prior}} - \boldsymbol{M}_k \tag{14}$$

$$\Delta \boldsymbol{D}_k = \boldsymbol{D_{prior}} - \boldsymbol{D}_k = \boldsymbol{D_{prior}} - F(\boldsymbol{M}_k) \tag{15}$$

To minimize Equation (13), pseudo-inverse can be applied as

$$\tilde{\boldsymbol{K}}^T_k = \left(\Delta \boldsymbol{D}^T_k \Delta \boldsymbol{D}_k \right)^{-1} (\Delta \boldsymbol{D}^T_k \Delta \boldsymbol{M}_k) \tag{16}$$

With the update direction $\tilde{\boldsymbol{K}}$, the model in the $(k+1)$th iteration is

$$\boldsymbol{M}_{k+1} = \boldsymbol{M}_k + \Delta \boldsymbol{D}_k \tilde{\boldsymbol{K}}^T_k \tag{17}$$

In practice, the difference between $\boldsymbol{D}$ and $\boldsymbol{D_{prior}}$ decreases rapidly. To stablize the training process, a regularization procedure is introduced [46]. Equation (16) becomes

$$\tilde{\boldsymbol{K}}^T_k = \left(\Delta \boldsymbol{D}^T_k \Delta \boldsymbol{D}_k + \alpha \boldsymbol{I} \right)^{-1} (\Delta \boldsymbol{D}^T_k \Delta \boldsymbol{M}_k) \tag{18}$$

where α is proportional to the largest singular value of $\Delta \boldsymbol{D}_k$ and $\boldsymbol{I}$ is the identity matrix.

Normalized model misfit is checked every iteration for validating training, which defined as

$$Rms_M(\boldsymbol{M}_k) = \frac{\|\Delta \boldsymbol{M}_k\|}{\|\boldsymbol{M_{prior}}\|} \tag{19}$$

3.3. Online Predicting Process

The online predicting process is to minimize the following function after offline training:

$$S^{Pr}(\Delta \boldsymbol{m}) = \left\| \Delta \boldsymbol{m} - \tilde{\boldsymbol{K}} \Delta \boldsymbol{d_{obs}} \right\|^2 \tag{20}$$

With the model update direction $\tilde{\boldsymbol{K}}$ obtained from offline training process, we can directly minimize Equation (20) as follows:

$$\boldsymbol{m}_{k+1} = \boldsymbol{m}_k + \tilde{\boldsymbol{K}} (\boldsymbol{d_{obs}} - F(\boldsymbol{m}_k)) \tag{21}$$

However, traveltime tomography is a ill-posed problem. The result obtained from Equation (21) might have artifacts. Here, Tikhonov regularization is applied to mitigate the ill-posedness [53]. New objective function can be written as

$$S^{Pr}_R(\boldsymbol{m}_{k+1}) = P(\boldsymbol{m}_{k+1}) + \alpha_v R_v(\boldsymbol{m}_{k+1}) + \alpha_h R_h(\boldsymbol{m}_{k+1}) \tag{22}$$

where

$$P(\boldsymbol{m}_{k+1}) = \left\| \boldsymbol{m}_{k+1} - \boldsymbol{m}_k - \tilde{\boldsymbol{K}}_k (\boldsymbol{d_{obs}} - F(\boldsymbol{m}_k)) \right\|^2 \tag{23}$$

$$R_v(\boldsymbol{m}_{k+1}) = \frac{\|\boldsymbol{d}_{obs} - F(\boldsymbol{m}_k)\|}{\|\boldsymbol{d}_{obs}\|} \int_\Omega \left(|\nabla_v \boldsymbol{m}_{k+1}|^2 + \delta_k^2 \right) d\boldsymbol{r} \tag{24}$$

$$R_h(\boldsymbol{m}_{k+1}) = \frac{\|\boldsymbol{d}_{obs} - F(\boldsymbol{m}_k)\|}{\|\boldsymbol{d}_{obs}\|} \int_\Omega \left(|\nabla_h \boldsymbol{m}_{k+1}|^2 + \delta_k^2 \right) d\boldsymbol{r} \tag{25}$$

$$\delta_k^2 = \frac{\|\boldsymbol{d}_{obs} - F(\boldsymbol{m}_k)\|^2}{\|\boldsymbol{d}_{obs}\|^2 \hat{\Delta}} \tag{26}$$

R_v and R_h are regularization terms along vertical and horizontal direction and they are proportional to the data misfit. $\hat{\Delta}$ is a positive real parameter related to the mesh size [54]. At the begining of the inversion, the data misfit is large and the regularization terms are strong, which prevents the appearing of extreme values and helps to converge to a better model. As the iteration goes on, the data misfit decreases and the model is closed to the local optimal model, regularization terms becomes weak and the model converges faster.

Equation (22) can be minimized directly as follow:

$$\frac{\partial S_R^{Pr}(\boldsymbol{m}_{k+1})}{\partial \boldsymbol{m}_{k+1}} = 0 \tag{27}$$

We have

$$\boldsymbol{m}_{k+1} = \boldsymbol{A}_{k+1}^{-1} \boldsymbol{b}_{k+1} \tag{28}$$

where

$$\boldsymbol{A}_{k+1} = \boldsymbol{I} + \frac{\|\boldsymbol{d}_{obs} - F(\boldsymbol{m}_k)\|}{\|\boldsymbol{d}_{obs}\|} \left(\alpha_v \nabla_v^T \nabla_v + \alpha_h \nabla_h^T \nabla_h \right) \tag{29}$$

$$\boldsymbol{b}_{k+1} = \boldsymbol{m}_k + \tilde{\boldsymbol{K}}_k (\boldsymbol{d}_{obs} - F(\boldsymbol{m}_k)) \tag{30}$$

Equation (28) is used to update the model every iteration during the inversion.

4. Numerical Experiments

In this section, details of the test domain and thorax model, settings of the training set and various numerical experiments will be discussed. In numerical experiments, our method is tested on a normal thorax model and synthetic thorax model of patients with respiratory diseases. It is also compared with the traditional gradient-based method on normal thorax model. All the numerical experiments are carried out with MATLAB R2020a on the same computer with Intel i5-6500 CPU, 32GB RAM.

4.1. Description of the Test Domain and Forward Modeling

The size of the test domain is 28.5 cm in length and 19 cm in width, and we divide it into 57 × 38 elements with length of 5 mm. The thorax model is shown in Figure 2, containing lung, heart, rib, spine, etc. [55]. The acoustic velocity of each tissue can be checked in [56]. The velocity of primary tissues in the thorax model is shown in Table 1. The blue background area is set to be water. The 22 black points mark the positions of the transducer. The transducer is labeled counterclockwise and the top-middle transducer in Figure 2 is the first one. Each transducer serves as the transmitter in turn and others serve as receivers. Totally $22 \times 21 = 462$ sets of traveltime data are obtained.

Table 1. The acoustic velocity of primary tissues in the thorax model.

Tissue	Acoustic Velocity (m/s)
Heart	1561
Lung (deflated)	1500
Bone (cancellous)	2117.5
Bone Marrow (yellow)	1371.9

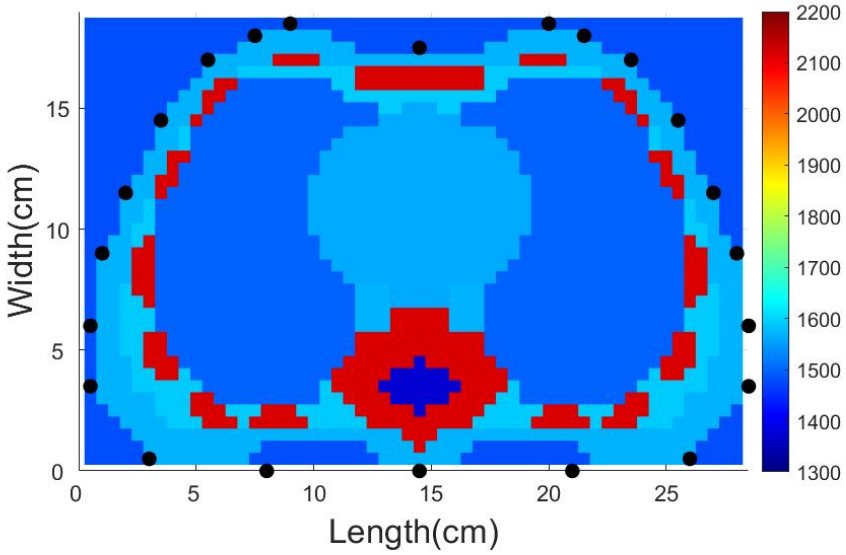

Figure 2. The thorax model in [55], containing lung, heart, rib, spine, etc. It is 28.5 cm in length and 19 cm in width. The blue background is set to be water. The black points around the thorax are where the transducers placed. The transducer is labeled counterclockwise and the top-middle transducer is the No. 1 transducer.

The number of nodes n_{nodes} on each edge of the element during the offline training process and online predicting process is chosen to be 3. n_{nodes} will influence the accuracy of the forward modeling and the time it takes. Increasing the number of nodes will improve the accuracy but at the same time increase the computation time. We calculate the traveltime data with $n_{nodes} = 1, 2, \ldots, 7$. The computation time for the forward modeling is shown in Figure 3a. We choose the traveltime obtained with $n_{nodes} = 7$ as the standard and calculate the relative error. Here, we plot the relative error of the traveltime data obtained from transmitter No. 6 in Figure 3b.

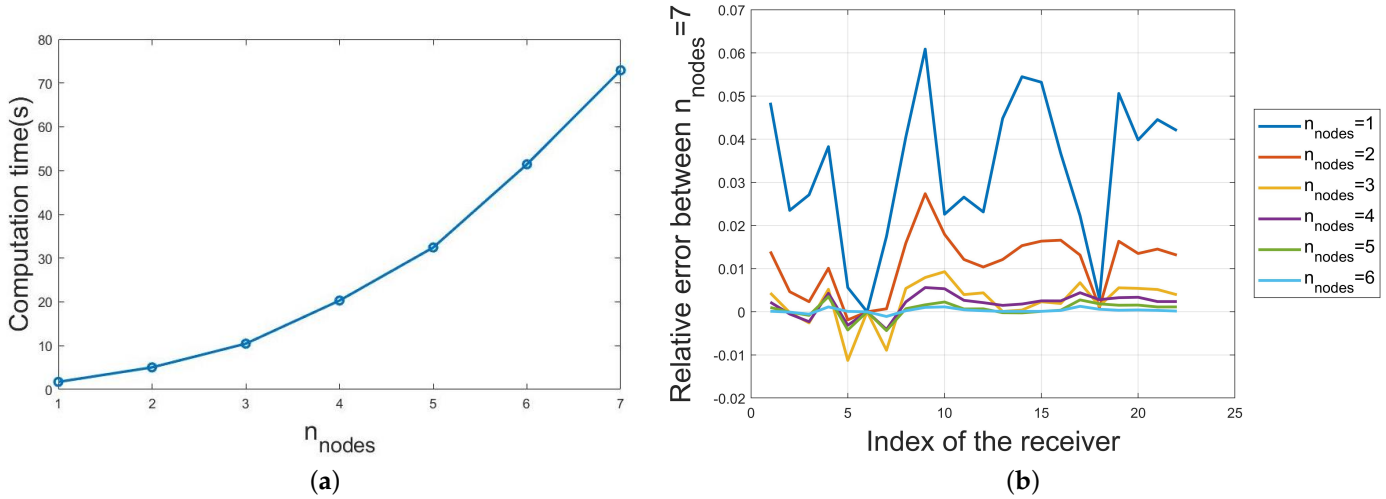

Figure 3. (**a**) Computation time of the forward modeling versus n_{nodes}. (**b**) The relative error of the traveltime data from transmitter No.6. The standard is the traveltime data obtained with $n_{nodes} = 7$.

When $n_{nodes} = 3$, the relative error of each data point is almost smaller than 0.01, which is small enough. If we keep increasing n_{nodes}, the decrease in the relative error is small, while the increase in the computation time is large. The computation time of $n_{nodes} = 4$ is almost twice as long as $n_{nodes} = 3$. In consideration of both efficiency and accuracy,

we choose $n_{nodes} = 3$. In addition, in order to avoid inverse crime, the traveltime data used for inversion in the following numerical experiments computed by SPR method is obtained from the grid with $n_{nodes} = 5$, because increasing n_{nodes} is equivalent to using a higher-resolution grid for forward modeling.

The distribution of the traveltime data obtained from normal thorax is shown in Figure 4. Maximum traveltime data are less than 180 μs. The median is 101.58 μs and its position is marked by the red line. To further avoid inverse crime, zero-mean white Gaussian noise with $\sigma = 2$ μs is added to the data.

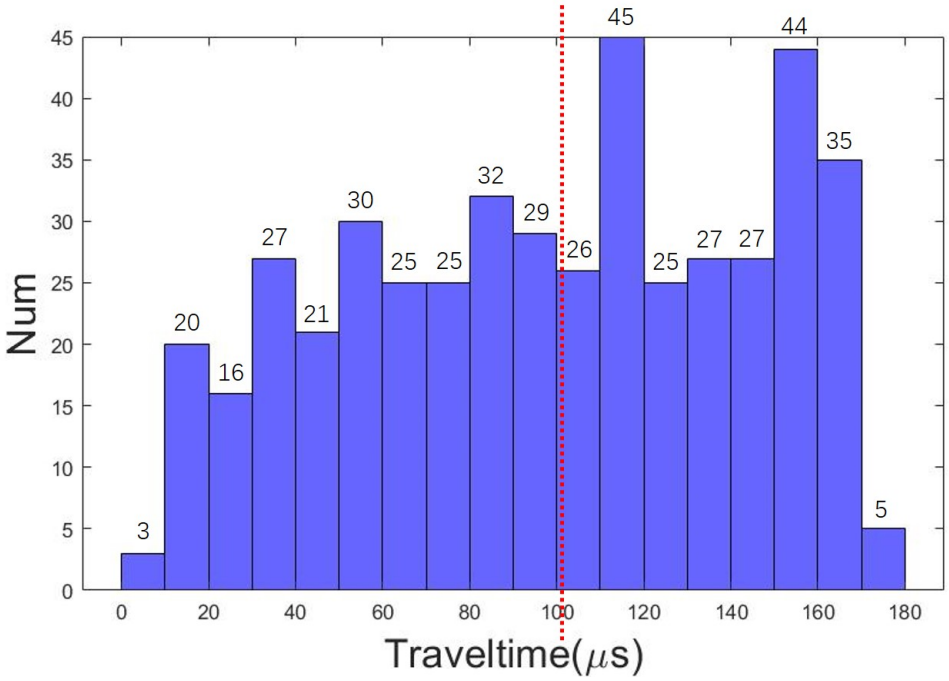

Figure 4. The distribution of 462 traveltime data. Maximum traveltime data is less than 180 μs. The red line marks the position of the median, which is 101.58 μs.

Then, we compare the traveltime data obtained from SPR method with the data obtained from k-Wave simulation [57]. We check tissues' density and attenuation coefficient in [56]. The thorax model is upsampled to 114 × 76 and put into a 128 × 128 domain with grid size of 2.5 mm. The timestep is set to be 0.25 μs and the simulation lasts for 500 μs. Gaussian waveform input signal is assigned to the transmitter and the rest transducers serve as receivers. We apply the Akaike information criteria (AIC) method to extract traveltime from the received waveform [58]. The transmitted waveform from transmitter No. 9 and the received waveform from receiver No.15 are shown in Figure 5. The position of the marker is calculated using AIC method. The distance between the two positions indicates the traveltime of the signal, which is 155.75 μs. The computed traveltime using the SPR method with $n_{nodes} = 3$ is 155.99 μs, which agrees well with the k-Wave simulation. The absolute value of the difference between the traveltime data computed by the SPR method and the k-Wave simulation is shown in Figure 6. Most are smaller than 2.5 μs, which verifies that the SPR method is accurate and can be used to compute traveltime in thorax imaging.

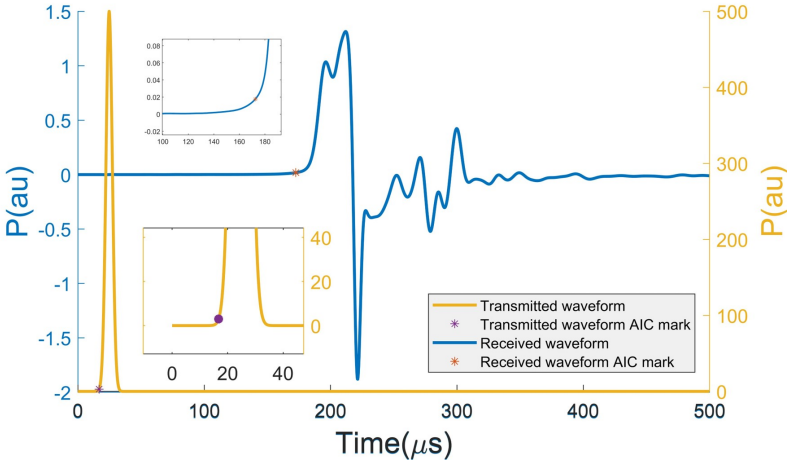

Figure 5. The transmitted waveform and the received waveform from transmitter No. 9 and receiver No. 15. The blue line is the received waveform corresponding to the left blue scale. The yellow line is the transmitted waveform corresponding to the right yellow scale. The position of the marker is calculated using AIC method, which marks the waveform is received/transmitted. The difference of the two positions is the traveltime of the signal, which is 155.75 µs.

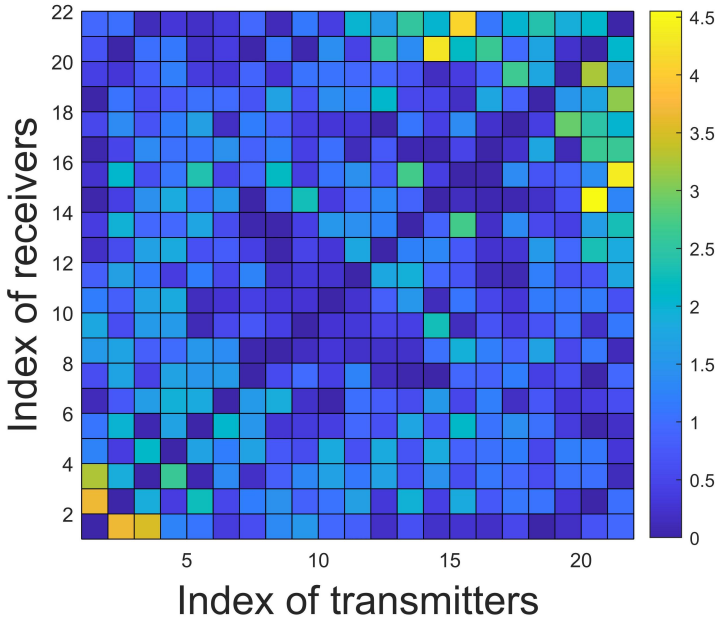

Figure 6. The absolute value of the traveltime data difference between SPR method with $n_{nodes} = 3$ and k-Wave simulation. Colorbar: 0–4.5 µs.

4.2. Details of the Training Set and the Training Process

When using the traditional gradient-based method to solve the traveltime tomography problem, the key step is computing the Jacobian matrix and the inverse of the Hessian matrix. However, only elements traversed by paths can be sensed in the traditional method. Usually, only few elements are traversed, which means the Hessian is generally sparse and hard to invert. In a traditional method, computing the inverse of Hessian needs the help of regularization and is time-consuming. To solve these problems, information of all the elements is added to the training set and the average descent direction is learned offline, which makes the online predicting fast and stable.

The training set is composed of a homogeneous low-velocity background (1500 m/s) and a high-velocity rectangular block (2200 m/s). The block has two sizes (4×8 and 8×4). The block moves one element at a time and covers the whole DoI (38×57) to make sure

that all the elements in the DoI are sensed. When moving to the edge of the DoI, the part of the block out of the region is cut. Totally $(38+7)\times(57+3)+(38+3)\times(57+7)=5324$ training models are generated. One of the training models is shown in Figure 7. Thus, the training process learns the sensitivity of traveltime with respect to velocity, which is inherently embedded with the prior knowledge on spatial correlations of velocity.

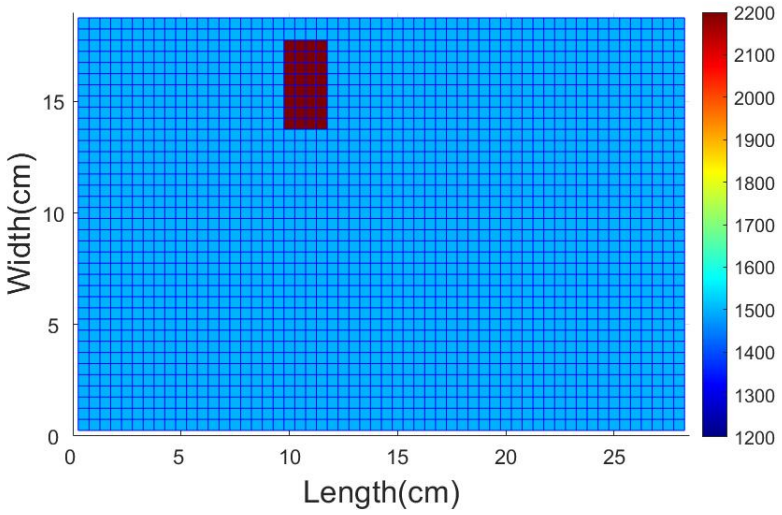

Figure 7. Example of the training model. Red Block: high-velocity block (2200 m/s). Blue region: low-velocity (1500 m/s) background.

During the training process, the initial model is set to be a homogeneous background with velocity of 1500 m/s. The maximum training step is set to be 5 for convenience. The predicting process will also last for 5 iterations and use the same initial value. The normalized model misfit is shown in Figure 8.

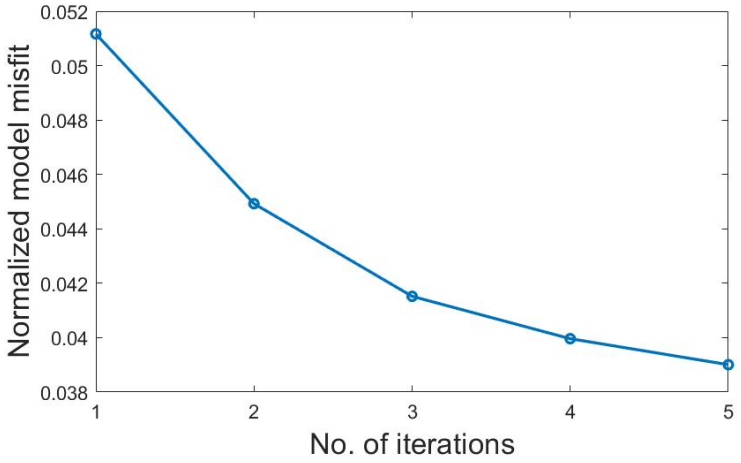

Figure 8. The normalized model misfit versus the No. of iterations in the training stage.

4.3. Numerical Experiments

In this section, all the simulated traveltime data are added with zero-mean white Gaussian noise with $\sigma = 2$ μs. The initial value of the inversion is a homogeneous background with acoustic velocity of 1500 m/s. The maximum iteration number is 5.

4.3.1. Comparison with Traditional Gradient-Based Method

The performance of SDM inversion is compared with traditional Gauss–Newton inversion. The ground truth is the thorax model shown in Figure 2. The results of the two methods are shown in Figure 9. We conduct inversion based on SPR method traveltime data and k-wave simulation traveltime data.

For inversion based on SPR method data, see Figure 9a,b. SDM finishes the inversion in 49.9 s. Although the Gauss–Newton method takes 102.9 s. SDM takes only half of the time the traditional method takes. In addition, from the results we find that the acoustic velocity distribution computed by SDM has fewer artifacts around the thorax and more precise tissue boundaries for ribs. The edges of lungs, ribs, and spine are clear. Heart and lungs are hard to distinguish because their acoustic velocity is close. However, both methods cannot correctly reconstruct the acoustic velocity of marrow because few paths traverse this region. According to Fermat's Principle, the wave will propagate along the path that takes the shortest time. The acoustic velocity of the marrow is significantly smaller than the spine around it, which means path would like to propagate in the spine rather than the marrow and result in low sensitivity of the marrow region. This example verifies the feasibility of imaging human thorax using ultrasound traveltime tomography with SDM. It also shows the strong generalization ability of SDM because little prior information on the shape of the thorax is added to the training set. The training model contains no structure information of thorax but only a rectangular high-velocity block and a homogeneous background. For inversion based on k-Wave simulation traveltime data, see Figure 9c,d, the results are similar to the inversion based on SPR method data, which further verifies the modeling and inversion algorithm. The traveltime data used in the following numerical experiment is all computed by SRP method with $n_{nodes} = 5$.

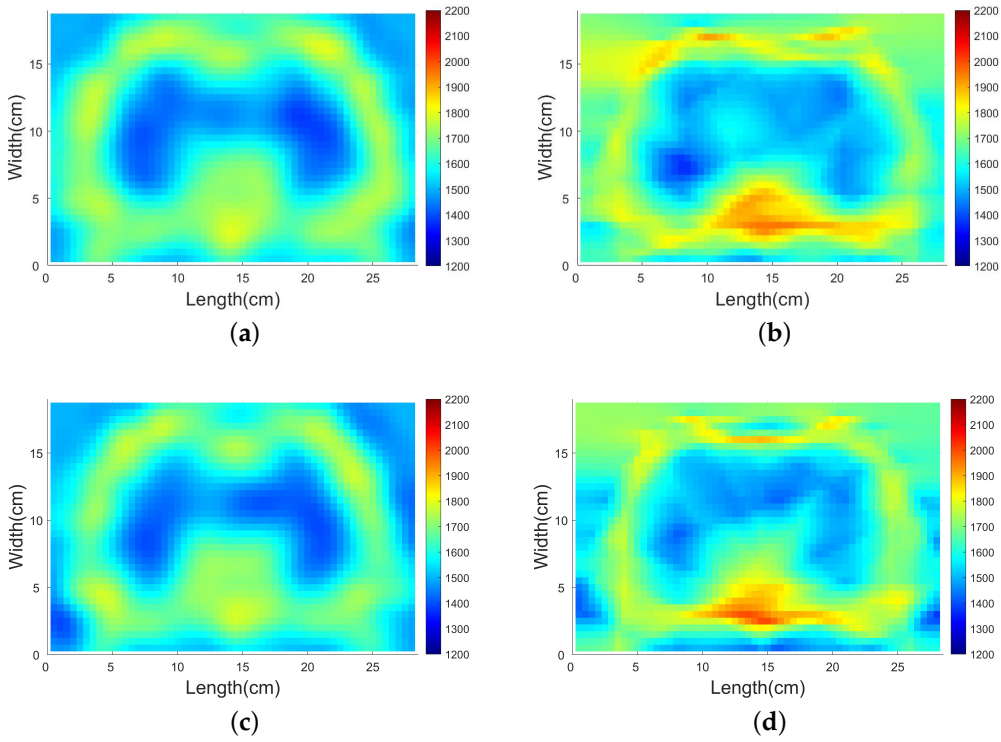

Figure 9. The inversion results of SDM inversion and Gauss–Newton inversion based on different traveltime data. (**a**) SDM inversion based on SPR method traveltime data, (**b**) Gauss–Newton inversion based on SPR method traveltime data, (**c**) SDM inversion based on k-Wave simulation traveltime data, (**d**) Gauss–Newton inversion based on k-Wave simulation traveltime data. Colorbar: 1200–2200 m/s. As a result (**a**), SDM takes 49.9 s to finish the inversion. As a result (**b**), the Gauss–Newton method takes 102.9 s.

A better initial model would help the inversion. The new initial model is obtained by smoothing the true model with a Gauss filter, see Figure 10a. The result of SDM inversion is shown in Figure 10b. Comparing the new result with the result shown in Figure 9a, we found that the area of the heart, marrow, and bones is better reconstructed. In the future, the initial model can be derived from CT or other imaging modalities.

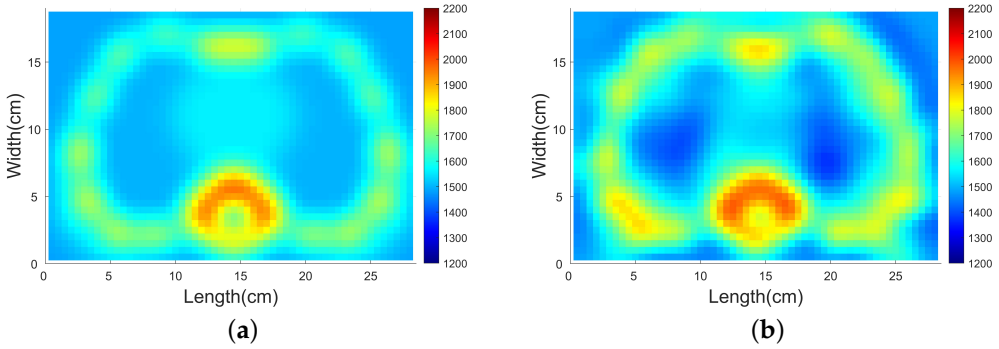

Figure 10. The new initial model and the resulf of SDM inversion. (**a**) The new initial model. (**b**) The result of SDM inversion. Colorbar: 1200–2200 m/s.

The inversion results cannot be improved by adding more transducers nor using a higher-resolution grid. We increase the number of transducers and the new array with 40 transducers is shown in Figure 11a. We also prepare a new grid whose size is 57×86. We conduct reconstruction on the same normal thorax model with previous array and new grid, new array and previous grid, and new array and new grid. New training sets are constructed for each task using the previous method. The inversion results are shown in Figure 11b–d. Compared with the inversion results shown in Figure 9b, no significant improvement can be seen. The reason the results have not improved might be that this traveltime tomography problem is too ill-posed. The current method cannot obtain the model out of the local minima. In addition, more transducers and higher-resolution grid will increase the time of inversion. The computation time of these three results is 132.9 s, 160.1 s, and 407.9 s, which are much longer than the previous 49.9 s.

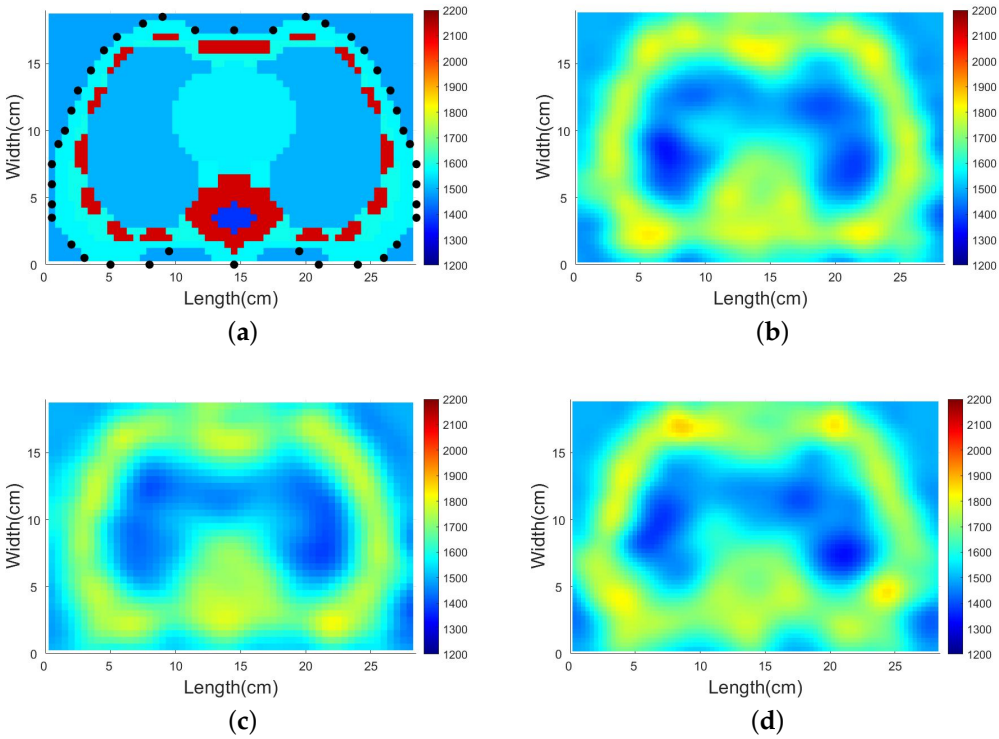

Figure 11. The new transucer array and the SDM inversion results with different array and different grid. (**a**) The new transducer array with 40 transducers, (**b**) inversion result with previous array and new grid, (**c**) inversion result with new array and previous grid, (**d**) inversion result with new array and new grid. Colorbar: 1200–2200 m/s.

4.3.2. SDM Traveltime Inversion of Thorax on Different States

Some respiratory system diseases might change the amount of gas and fluid in the thorax, which will cause changes in acoustic velocity because acoustic velocity in air is significantly smaller than in water. In this section, SDM traveltime tomography will be used to test whether these changes can be detected. Here, we take pleural effusion and pneumothorax as examples. Patients with pleural effusion tend to have more fluid in the thorax [59]. Although patients with pneumothorax will have more gas in the thorax [60].

Firstly, a pleural effusion patient's thorax acoustic velocity distribution is reconstructed, see the first column of Figure 12. We assume that the acoustic velocity of lungs when breathing in air will decrease to 1200 m/s (lower than average tissue acoustic velocity of 1540 m/s and higher than air acoustic velocity of 340 m/s). We suppose that the velocity distribution of a pleural effusion patient when breathing in air is like Figure 12a. The lower part of the left lung is the pleural effusion area. We suppose that the velocity of this area is 1540 m/s, same as the average tissue acoustic velocity. We want to reconstruct this high-velocity area near the low-velocity area through SDM traveltime tomography. The reconstruction result is shown in Figure 12c. The reconstruction result shows that both lungs' boundaries are clear and the left lung is smaller than the right one because the effusion area's velocity is higher than the normal lung area. For comparison, the result of the Gauss–Newton method is shown in Figure 12e, which has more artifacts. This example verifies that the change of acoustic velocity resulting from pleural effusion can be detected by SDM traveltime inversion.

Then, thorax acoustic velocity distribution of a pneumothorax patient is reconstructed, see the second column of Figure 12. We suppose that the velocity distribution of a pneumothorax patient when breathing out air is like Figure 12b. We suppose that the pneumothorax area is also located in the lower-left part of the thorax. The acoustic velocity of the pneumothorax area is assumed to be 1200 m/s, the same as the normal thorax region when breathing in air. In this example, a low-velocity region among high-velocity region will be reconstructed. The reconstruction result is shown in Figure 12d. The result shows that the boundaries of both lungs are clear and the pneumothorax area is reconstructed. The lower part of the left lung is darker than the lower part of the right lung. For comparison, the result of the Gauss–Newton method is shown in Figure 12f, where the boundary between normal area and pneumothorax area is not clear. This example verifies that the change of acoustic velocity resulting from pneumothorax can be detected by SDM traveltime inversion. In addition, the generalization ability of the method can also be demonstrated in these experiments. The learned descent direction can be applied to thorax under different conditions.

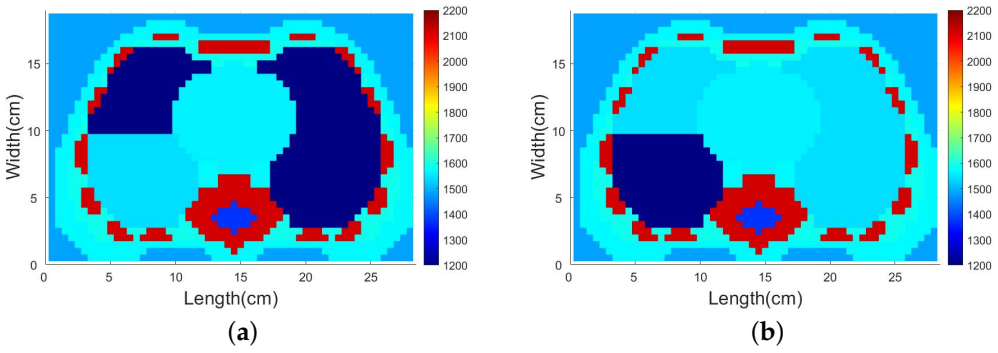

Figure 12. *Cont.*

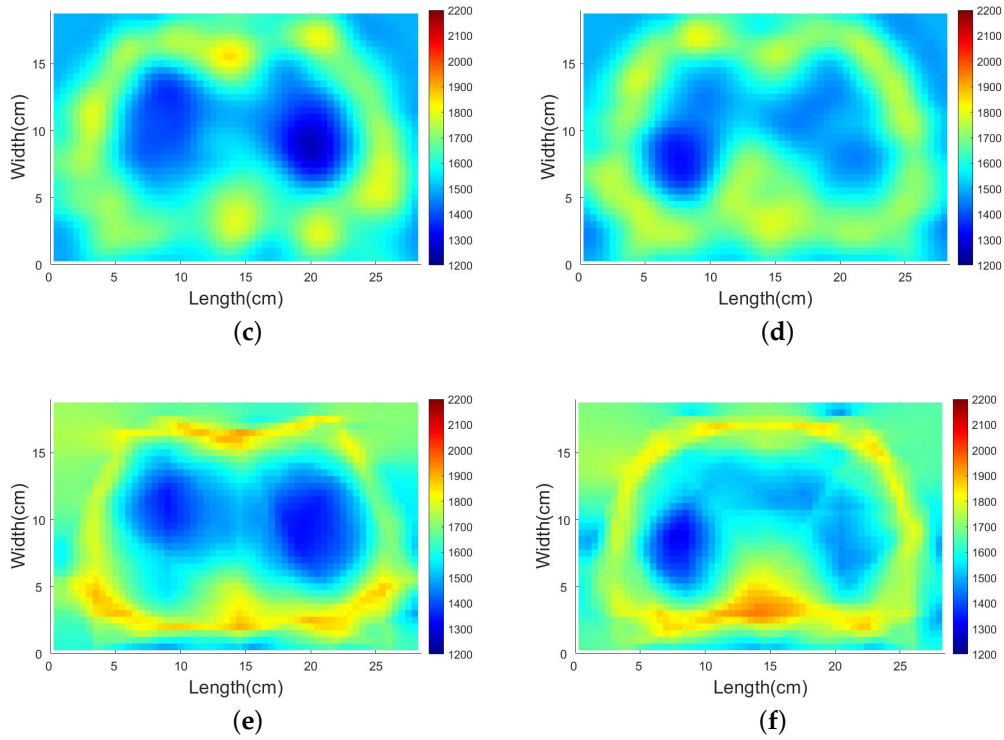

Figure 12. Thorax acoustic velocity distribution of a pleural effusion patient breathing in air and a pneumothorax patient breathing out air and the corresponding reconstruction results. (**a**) Thorax acoustic velocity distribution of a pleural effusion patient when breathing in air. (**b**) Thorax acoustic velocity distribution of a pneumothorax patient when breathing out air. (**c**) SDM inversion result of the thorax model (**a**). (**d**) SDM inversion result of the thorax model (**b**). (**e**) Gauss–Newton inversion result of the thorax model (**a**). (**f**) Gauss–Newton inversion result of the thorax model (**b**). Colorbar: 1200–2200 m/s.

5. Conclusions

In this paper, we verify the feasibility of imaging the human thorax using ultrasound traveltime tomography with SDM and detecting the change of acoustic velocity distribution resulting from respiratory diseases. A training set containing training models with homogeneous background and a high-velocity block covering the whole DoI is introduced. The average descent direction is learned from the training set and all elements in the DoI are sensed. Thanks to the offline training process, the online predicting process is fast and stable. In numerical experiments, SDM traveltime inversion is compared with the traditional gradient-based method on a normal thorax model. A slightly better result is obtained in half the time as the Gauss–Newton method, which means SDM traveltime inversion can be used to image human thorax efficiently. Then, we test its ability to detect the change in acoustic velocity distribution resulting from respiratory diseases. Thorax velocity distribution of pleural effusion and pneumothorax is assumed and inversed by our method. The results show that the synthetic change in acoustic velocity distribution can be detected. SDM also shows good generalization ability. No prior information about thorax structure is added to the training set and the learned descent direction can be applied to inverse thorax at different states. Computing the acoustic velocity distribution can help to monitor human respiratory system, as the acoustic velocity is closely related to tissues' physical properties. In conclusion, ultrasound traveltime tomography with SDM can be used to image human thorax and detect the change in thorax acoustic velocity distribution efficiently. It might be helpful for the diagnosis and quantitative evaluation of respiratory diseases and the localization of the lesion area.

Author Contributions: Project administration, T.Z., M.L., F.Y. and S.X.; Resources, T.Z.; software, T.Z., R.G., H.Z. (Hongyu Zhou), H.Z. (Haolin Zhang) and Y.C.; Supervision, M.L.; Writing—original draft preparation, T.Z. All authors have read and agreed to the published version of the manuscript.

Funding: This research was funded by National Natural Science Foundation of China (61971263), the National Key R&D Program of China (2018YFC0603604), and Institute for Precision Medicine, Tsinghua University, Beijing, China, and Biren Tech, Beijing, China.

Conflicts of Interest: The authors declare no conflict of interest.

Abbreviations

The following abbreviations are used in this manuscript:

SDM	Supervised Descent Method
SPR	Shortest Path Ray
DoI	Domain of Interest
NDE	Nondestructive Evaluation
CT	Computed Tomography
MRI	Magnetic Resonance Imaging
SNR	Signal to Noise Ratio
EIT	Electrical Impedance Tomography

References

1. Chiao, R.Y.; Thomas, L.J. Analytic evaluation of sampled aperture ultrasonic imaging techniques for NDE. *IEEE Trans. Ultrason. Ferroelectr. Freq. Control* **1994**, *41*, 484–493. [CrossRef]
2. Sun, H.; Zhu, J. Nondestructive evaluation of steel-concrete composite structure using high-frequency ultrasonic guided wave. *Ultrasonics* **2020**, *103*, 106096. [CrossRef]
3. Liu, H.; Xia, H.; Zhuang, M.; Long, Z.; Liu, C.; Cui, J.; Xu, B.; Hu, Q.; Liu, Q.H. Reverse time migration of acoustic waves for imaging based defects detection for concrete and CFST structures. *Mech. Syst. Signal Process.* **2019**, *117*, 210–220. [CrossRef]
4. Gardner, P.; Fuentes, R.; Dervilis, N.; Mineo, C.; Pierce, S.; Cross, E.; Worden, K. Machine learning at the interface of structural health monitoring and non-destructive evaluation. *Philos. Trans. R. Soc. A* **2020**, *378*, 20190581. [CrossRef] [PubMed]
5. Ricciardi, L.; Perissinotto, A.; Dabala, M. Mechanical monitoring of fracture healing using ultrasound imaging. *Clin. Orthop. Relat. Res.* **1993**, *293*, 71–76. [CrossRef]
6. Dong, F.; Jiang, Z.; Qiao, X.; Xu, L. Application of electrical resistance tomography to two-phase pipe flow parameters measurement. *Flow Meas. Instrum.* **2003**, *14*, 183–192. [CrossRef]
7. Tan, C.; Li, X.; Liu, H.; Dong, F. An ultrasonic transmission/reflection tomography system for industrial multiphase flow imaging. *IEEE Trans. Ind. Electron.* **2019**, *66*, 9539–9548. [CrossRef]
8. Yang, M.; Schlaberg, H.I.; Hoyle, B.S.; Beck, M.S.; Lenn, C. Real-time ultrasound process tomography for two-phase flow imaging using a reduced number of transducers. *IEEE Trans. Ultrason. Ferroelectr. Freq. Control* **1999**, *46*, 492–501. [CrossRef]
9. Gonçalves, L.F.; Espinoza, J.; Romero, R.; Kusanovic, J.P.; Swope, B.; Nien, J.K.; Erez, O.; Soto, E.; Treadwell, M.C. Four-dimensional ultrasonography of the fetal heart using a novel Tomographic Ultrasound Imaging display. *J. Perinat. Med.* **2006**, *34*, 39–55. [CrossRef]
10. Brekke, S.; Tegnander, E.; Torp, H.; Eik-Nes, S. Tissue Doppler gated (TDOG) dynamic three-dimensional ultrasound imaging of the fetal heart. *Ultrasound Obstet. Gynecol. Off. J. Int. Soc. Ultrasound Obstet. Gynecol.* **2004**, *24*, 192–198. [CrossRef]
11. Papadacci, C.; Finel, V.; Villemain, O.; Tanter, M.; Pernot, M. 4D ultrafast ultrasound imaging of naturally occurring shear waves in the human heart. *IEEE Trans. Med. Imaging* **2020**, *39*, 4436–4444. [CrossRef] [PubMed]
12. Xue, L.Y.; Jiang, Z.Y.; Fu, T.T.; Wang, Q.M.; Zhu, Y.L.; Dai, M.; Wang, W.P.; Yu, J.H.; Ding, H. Transfer learning radiomics based on multimodal ultrasound imaging for staging liver fibrosis. *Eur. Radiol.* **2020**, *30*, 2973–2983. [CrossRef] [PubMed]
13. Berzigotti, A.; Castera, L. Update on ultrasound imaging of liver fibrosis. *J. Hepatol.* **2013**, *59*, 180–182. [CrossRef] [PubMed]
14. Imbault, M.; Chauvet, D.; Gennisson, J.L.; Capelle, L.; Tanter, M. Intraoperative functional ultrasound imaging of human brain activity. *Sci. Rep.* **2017**, *7*, 7304. [CrossRef]
15. Demene, C.; Baranger, J.; Bernal, M.; Delanoe, C.; Auvin, S.; Biran, V.; Alison, M.; Mairesse, J.; Harribaud, E.; Pernot, M.; et al. Functional ultrasound imaging of brain activity in human newborns. *Sci. Transl. Med.* **2017**, *9*, eaah6756. [CrossRef]
16. Macé, E.; Montaldo, G.; Cohen, I.; Baulac, M.; Fink, M.; Tanter, M. Functional ultrasound imaging of the brain. *Nat. Methods* **2011**, *8*, 662–664. [CrossRef]
17. Szabo, T.L. *Diagnostic Ultrasound Imaging: Inside Out*; Academic Press: Cambridge, MA, USA, 2004.
18. Zhou, B.; Yang, X.; Zhang, X.; Curran, W.J.; Liu, T. Ultrasound elastography for lung disease assessment. *IEEE Trans. Ultrason. Ferroelectr. Freq. Control.* **2020**, *67*, 2249–2257. [CrossRef]

19. Wang, X.; Peng, Y.; Lu, L.; Lu, Z.; Bagheri, M.; Summers, R.M. Chestx-ray8: Hospital-scale chest X-ray database and benchmarks on weakly-supervised classification and localization of common thorax diseases. In Proceedings of the IEEE Conference on Computer Vision and Pattern Recognition, Honolulu, HI, USA, 21–26 July 2017; pp. 2097–2106.
20. Nehmeh, S.; Erdi, Y.; Pan, T.; Pevsner, A.; Rosenzweig, K.; Yorke, E.; Mageras, G.; Schoder, H.; Vernon, P.; Squire, O.; et al. Four-dimensional (4D) PET/CT imaging of the thorax: 4D PET/CT. *Med. Phys.* **2004**, *31*, 3179–3186. [CrossRef]
21. Ates, O.F.; Taydas, O.; Dheir, H. Thorax magnetic resonance imaging findings in patients with coronavirus disease (COVID-19). *Acad. Radiol.* **2020**, *27*, 1373–1378. [CrossRef]
22. Zhang, K.; Li, M.; Yang, F.; Xu, S.; Abubakar, A. Three-dimensional electrical impedance tomography with multiplicative regularization. *IEEE Trans. Biomed. Eng.* **2019**, *66*, 2470–2480. [CrossRef]
23. Zhang, H.; Li, M.; Yang, F.; Xu, S.; Zhou, H.; Yang, Y.; Chen, L. A low-profile compact dual-band l-shape monopole antenna for microwave thorax monitoring. *IEEE Antennas Wirel. Propag. Lett.* **2020**, *19*, 448–452. [CrossRef]
24. Martelius, L.; Heldt, H.; Lauerma, K. B-lines on pediatric lung sonography: Comparison with computed tomography. *J. Ultrasound Med.* **2016**, *35*, 153–157. [CrossRef] [PubMed]
25. Mento, F.; Soldati, G.; Prediletto, R.; Demi, M.; Demi, L. Quantitative lung ultrasound spectroscopy applied to the diagnosis of pulmonary fibrosis: The first clinical study. *IEEE Trans. Ultrason. Ferroelectr. Freq. Control* **2020**, *67*, 2265–2273. [CrossRef] [PubMed]
26. Dargent, A.; Chatelain, E.; Kreitmann, L.; Quenot, J.P.; Cour, M.; Argaud, L.; COVID-LUS Study Group. Lung ultrasound score to monitor COVID-19 pneumonia progression in patients with ARDS. *PLoS ONE* **2020**, *15*, e0236312. [CrossRef]
27. Wang, G.; Ji, X.; Xu, Y.; Xiang, X. Lung ultrasound: A promising tool to monitor ventilator-associated pneumonia in critically ill patients. *Crit. Care* **2016**, *20*, 1–10. [CrossRef]
28. Buonsenso, D.; Brancato, F.; Valentini, P.; Curatola, A.; Supino, M.; Musolino, A.M. The use of lung ultrasound to monitor the antibiotic response of community-acquired pneumonia in children: A preliminary hypothesis. *J. Ultrasound Med.* **2020**, *39*, 817–826. [CrossRef]
29. Rueter, D.; Hauber, H.P.; Droeman, D.; Zabel, P.; Uhlig, S. Low-frequency ultrasound permeates the human thorax and lung: A novel approach to non-invasive monitoring. *Ultraschall Der Med.-Eur. J. Ultrasound* **2010**, *31*, 53–62. [CrossRef]
30. Dai, Z.; Peng, Y.; Mansy, H.A.; Sandler, R.H.; Royston, T.J. Comparison of poroviscoelastic models for sound and vibration in the lungs. *J. Vib. Acoust.* **2014**, *136*, 050905. [CrossRef]
31. Peng, Y.; Dai, Z.; Mansy, H.A.; Henry, B.M.; Sandler, R.H.; Balk, R.A.; Royston, T.J. Sound transmission in porcine thorax through airway insonification. *Med. Biol. Eng. Comput.* **2016**, *54*, 675–689. [CrossRef]
32. Mansy, H.A.; Balk, R.A.; Warren, W.H.; Royston, T.J.; Dai, Z.; Peng, Y.; Sandler, R.H. Pneumothorax effects on pulmonary acoustic transmission. *J. Appl. Physiol.* **2015**, *119*, 250–257. [CrossRef]
33. Palnitkar, H.; Henry, B.M.; Dai, Z.; Peng, Y.; Mansy, H.A.; Sandler, R.H.; Balk, R.A.; Royston, T.J. Sound transmission in human thorax through airway insonification: An experimental and computational study with diagnostic applications. *Med. Biol. Eng. Comput.* **2020**, *58*, 2239–2258. [CrossRef] [PubMed]
34. Morenz, K.; Biller, H.; Wolfram, F.; Leonhadt, S.; Rüter, D.; Glaab, T.; Uhlig, S.; Hohlfeld, J.M. Detection of air trapping in chronic obstructive pulmonary disease by low frequency ultrasound. *BMC Pulm. Med.* **2012**, *12*, 8. [CrossRef] [PubMed]
35. Pohlmann, A.; Sehati, S.; Young, D. Effect of changes in lung volume on acoustic transmission through the human respiratory system. *Physiol. Meas.* **2001**, *22*, 233. [CrossRef] [PubMed]
36. Li, C.; Duric, N.; Littrup, P.; Huang, L. In vivo breast sound-speed imaging with ultrasound tomography. *Ultrasound Med. Biol.* **2009**, *35*, 1615–1628. [CrossRef] [PubMed]
37. Duric, N.; Littrup, P.; Poulo, L.; Babkin, A.; Pevzner, R.; Holsapple, E.; Rama, O.; Glide, C. Detection of breast cancer with ultrasound tomography: First results with the Computed Ultrasound Risk Evaluation (CURE) prototype. *Med. Phys.* **2007**, *34*, 773–785. [CrossRef]
38. Zhang, H.; Thurber, C.; Rowe, C. Automatic P-wave arrival detection and picking with multiscale wavelet analysis for single-component recordings. *Bull. Seismol. Soc. Am.* **2003**, *93*, 1904–1912. [CrossRef]
39. Li, C.; Huang, L.; Duric, N.; Zhang, H.; Rowe, C. An improved automatic time-of-flight picker for medical ultrasound tomography. *Ultrasonics* **2009**, *49*, 61–72. [CrossRef]
40. Fatemi, A.; Måsøy, S.E.; Rodriguez-Molares, A. Row–Column-Based Coherence Imaging Using a 2-D Array Transducer: A Row-Based Implementation. *IEEE Trans. Ultrason. Ferroelectr. Freq. Control* **2020**, *67*, 2303–2311. [CrossRef]
41. Wodicka, G.R.; Stevens, K.N.; Golub, H.L.; Cravalho, E.G.; Shannon, D.C. A model of acoustic transmission in the respiratory system. *IEEE Trans. Biomed. Eng.* **1989**, *36*, 925–934. [CrossRef]
42. Picano, E.; Pellikka, P.A. Ultrasound of extravascular lung water: A new standard for pulmonary congestion. *Eur. Heart J.* **2016**, *37*, 2097–2104. [CrossRef]
43. Porcel, J.M.; Light, R.W. Pleural effusions due to pulmonary embolism. *Curr. Opin. Pulm. Med.* **2008**, *14*, 337–342. [CrossRef] [PubMed]
44. Xiong, X.; De la Torre, F. Supervised descent method and its applications to face alignment. In Proceedings of the IEEE Conference on Computer Vision and Pattern Recognition, Portland, OR, USA, 23–28 June 2013; pp. 532–539.
45. Guo, R.; Li, M.; Yang, F.; Xu, S.; Abubakar, A. Application of supervised descent method for 2D magnetotelluric data inversion. *Geophysics* **2020**, *85*, WA53–WA65. [CrossRef]

46. Zhang, H.; Li, M.; Yang, F.; Xu, S.; Yin, Y.; Zhou, H.; Yang, Y.; Zeng, S.; Shao, J. A feasibility study of 2-d microwave thorax imaging based on the supervised descent method. *Electronics* **2021**, *10*, 352. [CrossRef]
47. Zhang, K.; Guo, R.; Li, M.; Yang, F.; Xu, S.; Abubakar, A. Supervised descent learning for thoracic electrical impedance tomography. *IEEE Trans. Biomed. Eng.* **2020**, *68*, 1360–1369. [CrossRef]
48. Lin, M.; Liu, Y. Guided Wave Tomography Based on Supervised Descent Method for Quantitative Corrosion Imaging. *IEEE Trans. Ultrason. Ferroelectr. Freq. Control* **2021**, *68*, 3624–3636. [CrossRef]
49. Rawlinson, N.; Sambridge, M. Seismic traveltime tomography of the crust and lithosphere. *Adv. Geophys.* **2003**, *46*, 81–199.
50. Moser, T. Shortest path calculation of seismic rays. *Geophysics* **1991**, *56*, 59–67. [CrossRef]
51. Zhang, H.; Zhang, T.; Zhou, H.; Li, M.; Yang, F.; Xu, S.; Cao, Y. A Preliminary Experiment Based on One-step Measurement-trained Supervised Descent Method for Microwave Thorax Imaging. In Proceedings of the 2021 Photonics & Electromagnetics Research Symposium (PIERS), Hangzhou, China, 21–25 November 2021; pp. 1921–1930.
52. Guo, R.; Li, M.; Yang, F.; Xu, S.; Abubakar, A. First arrival traveltime tomography using supervised descent learning technique. *Inverse Probl.* **2019**, *35*, 105008. [CrossRef]
53. Tikhonov, A.N.; Arsenin, V.Y. *Solutions of Ill-Posed Problems*; VH Winston & Sons: New York, NY, USA, 1977.
54. Song, X.; Li, M.; Yang, F.; Xu, S.; Abubakar, A. Feasibility study of acoustic imaging for human thorax using an acoustic contrast source inversion algorithm. *J. Acoust. Soc. Am.* **2018**, *144*, 2782–2792. [CrossRef]
55. Song, X.; Li, M.; Yang, F.; Xu, S.; Abubakar, A. Study on joint inversion algorithm of acoustic and electromagnetic data in biomedical imaging. *IEEE J. Multiscale Multiphysics Comput. Tech.* **2019**, *4*, 2–11. [CrossRef]
56. Hasgall, P.; Di Gennaro, F.; Baumgartner, C.; Neufeld, E.; Lloyd, B.; Gosselin, M.; Payne, D.; Klingenböck, A.; Kuster, N. *IT'IS Database for Thermal and Electromagnetic Parameters of Biological Tissues*; version 4.1; Elsevier: Boston, FL, USA, 2022.
57. Treeby, B.E.; Budisky, J.; Wise, E.S.; Jaros, J.; Cox, B. Rapid calculation of acoustic fields from arbitrary continuous-wave sources. *J. Acoust. Soc. Am.* **2018**, *143*, 529–537. [CrossRef] [PubMed]
58. Maeda, N. A method for reading and checking phase times in autoprocessing system of seismic wave data. *Zisin* **1985**, *38*, 365–379. [CrossRef]
59. Kuhlman, J.E.; Singha, N.K. Complex disease of the pleural space: Radiographic and CT evaluation. *Radiographics* **1997**, *17*, 63–79. [CrossRef] [PubMed]
60. Currie, G.P.; Alluri, R.; Christie, G.L.; Legge, J.S. Pneumothorax: An update. *Postgrad. Med. J.* **2007**, *83*, 461–465. [CrossRef] [PubMed]